HIGH-FIDELITY COMPUTATIONAL STUDY OF ROUGHNESS EFFECTS ON HIGH PRESSURE TURBINE PERFORMANCE AND HEAT TRANSFER

Thomas O. Jelly
School of Engineering
University of Leicester
LE1 7RH, United Kingdom
tj119@leicester.ac.uk

Massimiliano Nardini
Department of Mechanical Engineering
University of Melbourne
Victoria 3010, Australia
mnardini@unimelb.edu.au

Marco Rosenzweig
Department of Mechanical Engineering
University of Melbourne
Victoria 3010, Australia
marco.rosenzweig@unimelb.edu.au

John Leggett
Department of Mechanical Engineering
University of Melbourne
Victoria 3010, Australia
jake.leggett@unimelb.edu.au

Ivan Marusic
Department of Mechanical Engineering
University of Melbourne
Victoria 3010, Australia
imarusic@unimelb.edu.au

Richard D. Sandberg
Department of Mechanical Engineering
University of Melbourne
Victoria 3010, Australia
richard.sandberg@unimelb.edu.au

ABSTRACT

A series of high-resolved Large-Eddy Simulations (LES) of the LS89 high-pressure turbine (HPT) vane with systematically varied levels of blade surface roughness have been performed. Three roughness amplitudes have been investigated, namely, $k_s/c = \{1.0, 2.0, 3.0\} \times 10^{-3}$, where k_s is an equivalent value of Nikuradse's sandgrain roughness for a near-Gaussian height distribution, and c is the axial blade chord. A reference smooth-blade simulation at matched flow conditions was also conducted for comparison. All simulations have been performed at a chord Reynolds number of 0.59×10^6 and Mach number of 0.9, based on the exit conditions of the reference smooth vane, and with synthetic inflow turbulence to mimic incoming disturbances from an upstream combustion chamber. The data presented here highlight the strong aero-thermal effect that blade surface roughness has not only upon boundary-layer transition mechanisms on the blade suction-side but also on wall shear stress and wall heat flux, as well as the levels of turbulence kinetic energy and total pressure loss in the wake.

INTRODUCTION

Blade surface roughness ranks amongst the most critical factors affecting high pressure turbine (HPT) aero-thermal performance and is especially relevant in the case of in-service degradation (Bons, 2010) and additively manufactured components (McClain *et al.*, 2021). Whilst it is well-known that blade surface roughness can increase heat transfer and pressure losses well above aerodynamically smooth levels (Bons, 2002), the detailed underlying mechanisms remain far from fully understood — particularly in realistic environments at high Reynolds and Mach numbers featuring strong pressure gradients and surface curvature. Furthermore, although empirical models have been proposed to account for roughness effects (Stripf *et al.*, 2008), predictive models that faithfully reproduce blade boundary-layer dynamics and the associated loss mechanisms in engine-relevant operating conditions remain elusive.

Whilst computational fluid dynamics (CFD) is a key design tool in gas turbine (GT) development, its potential is far from being fully realised due to challenges in simulation and modelling of aero-thermal performance in realistic environments (Sandberg & Michelassi, 2022). In practice, design iterations are accomplished by modelling all scales of turbulence with the well-known Reynolds Averaged Navier-Stokes (RANS) and Unsteady RANS (URANS) equations. While fast and robust, RANS and URANS can suffer from accuracy issues in the presence of complex mixing processes (Michelassi *et al.*, 1998; Pichler *et al.*, 2016) or blade surface roughness effects (Joo *et al.*, 2016). Considering that just a 2% error in the predicted metal temperature is estimated to halve the effective blade life (Han *et al.*, 2012), detailed analysis of roughness effects in HPT flows is necessary not only to gain deeper insight of the fundamental flow physics, but also to more accurately predict pressure losses and heat transfer.

High-fidelity simulations, including both Direct Numerical Simulation and Large-Eddy Simulation (LES), have been shown to be very accurate in simulating flow past smooth HPT vanes (Bhaskaran & Lele, 2010; Jee *et al.*, 2016; Zhao & Sandberg, 2020). On the other hand, high-fidelity simulations of flow past rough HPT vanes remain very limited. To date, most past work has focussed on roughness effects in low pressure turbines (Hammer *et al.*, 2018) or non-equilbrium flatplate boundary-layers (Vadlamani *et al.*, 2018), at significantly lower Reynolds number. As a result, several questions regarding the fundamental mechanisms that govern the aero-thermal performance of HPTs remain open.

The present study complements this past work by studying surface roughness effects upon the aero-thermal performance of the LS89 HPT vane using a high-fidelity computational approach for the very first time. Particular attention is drawn towards how systematically varying the levels of surface roughness affects the dynamics of laminar-turbulence transition on the blade suction side and its associated impact upon wall shear stress and wall heat flux, as well as the levels of turbulence kinetic energy and total pressure losses in the wake of the HPT blade.

COMPUTATIONAL METHODOLOGY

Large-Eddy Simulations (LES) were performed using an in-house multi-block structured curvilinear compressible Navier-Stokes solver called HiPSTAR (Sandberg *et al.*, 2015) that uses higher-order numerical methods optimised for performance on the world's fastest supercomputers. For the cases reported herein, simulations were undertaken using a minimum of 576 Nvidia V100 GPUs of the Summit supercomputer at Oak Ridge National Laboratory. Spatial discretisation is achieved using fourth-order wavenumber-optimised compact finite differences. An ultra-low storage frequency optimised fourth-order explicit Runge-Kutta method is used for time advancement. The subgrid-scale contribution is provided by the WALE model (Nicoud & Ducros, 1999) with a standard coefficient of $C_w = 0.325$. The present study employs the same overset mesh configuration devised by Zhao & Sandberg (2021), which consists of an O-type grid wrapped around the HPT blade embedded into a background H-type grid. A schematic of the overset grid configuration is shown in Figure 1a. Whilst HiPSTAR has been used extensively to perform LES of HPT flows (Pichler *et al.*, 2017; Zhao & Sandberg, 2020, 2021), these past studies have focussed on smooth blade geometries that were explicitly resolved using body-fitted grids. In the present study, the roughened blade geometries are represented using a second-order accurate boundary data immersion method (BDIM) (Schlanderer *et al.*, 2017).

The blade surface roughness under consideration here is irregular, three-dimensional and near-Gaussian. According to Bons (2002), near-Gaussian roughness on turbine blades develops as a result of metal erosion mechanisms, whereas non-Gaussian roughness develops due to thermal barrier coating spallation or pitting. The Gaussian height distribution used in the present study was synthesised using an algorithm devised in past work by Jelly & Busse (2018, 2019), which generates irregular roughness with doubly periodic boundary conditions by taking weighted linear combinations of Gaussian random number matrices using a moving average process. So far, three roughness amplitudes have been investigated, namely, $k_s/c = \{1.0, 2.0, 3.0\} \times 10^{-3}$, where k_s is an equivalent value of Nikuradse's sandgrain roughness and c is the axial blade chord. Here, k_s is related to the r.m.s. roughness height, k_{rms}, through the scaling factor $C \equiv k_s/k_{rms} = 5.0$. Close-up views of the trailing edge (TE) surface roughness for each value of k_s/c are shown in Figure 2. According to Bons (2010), the effects of blade surface roughness become admissible above $k_s/c \approx 1 \times 10^{-4}$. Hence, the roughness under investigation here is anticipated to have an appreciable aero-thermal effect.

In the LES, the BDIM algorithm is used to apply no-slip isothermal boundary conditions on the roughened blade surface. A discrete representation of the three-dimensional blade geometry is immersed in a "roughness layer" that extends above and below the roughness mean plane, which coincides with the coordinates of the smooth HPT vane. The roughness layer was resolved using a minimum of 140 grid points which were spaced equally in the blade-normal direction. Above the roughness layer the blade-normal grid spacing is gradually increased, reaching a maximum value at the outer edge of the embedded O-type grid. A schematic of the roughness layer in the TE region is shown in Figure 1b.

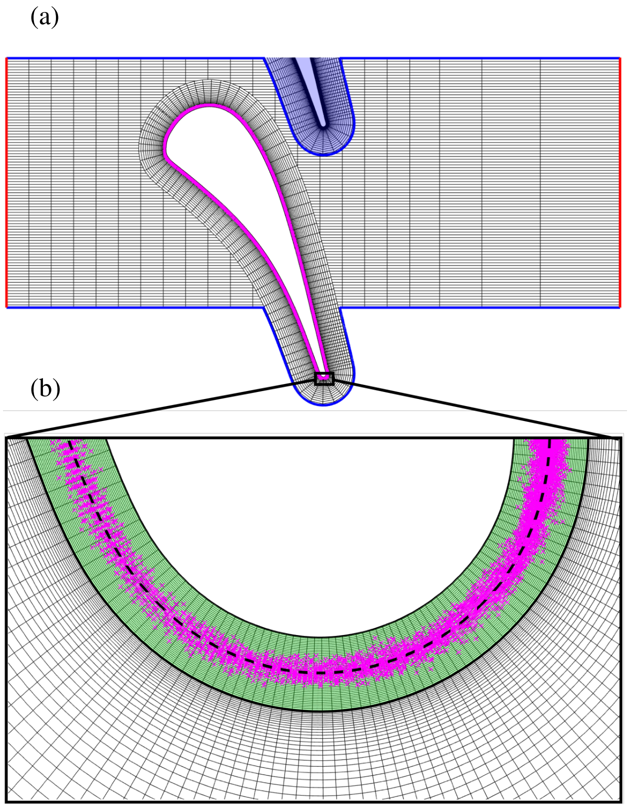

Figure 1. (a) Schematic of the overset mesh setup showing the curvilinear O-type grid around blade embedded into the background Cartesian H-type grid. For clarity, only every 64$^{\text{th}}$ and 8$^{\text{th}}$ grid point is shown in the streamwise and pitchwise direction, respectively. Pitchwise periodic boundaries are highlighted as solid blue lines (——) and the inlet and outlet planes are highlighted as solid red lines (——). (b) Zoomed-in view of the blade trailing edge, illustrating the pitchwise extent of the roughness layer (shaded green area), where the discrete three-dimensional point cloud of the roughened HPT blade (×) is immersed in a constant mesh spacing region. The mean blade coordinates are shown as the black dashed line (- - -). For clarity, only every 6$^{\text{th}}$ and 3$^{\text{rd}}$ grid point is shown in the streamwise and pitchwise direction, respectively.

For each roughness amplitude, an LES was performed at at a chord Reynolds number of $Re = 0.59 \times 10^6$ and Mach number of $Ma = 0.9$, based on the exit conditions of the reference smooth vane. The width of the computational domain in the spanwise direction was set equal to 40% of the axial blade chord, which is wide enough to ensure that the turbu-

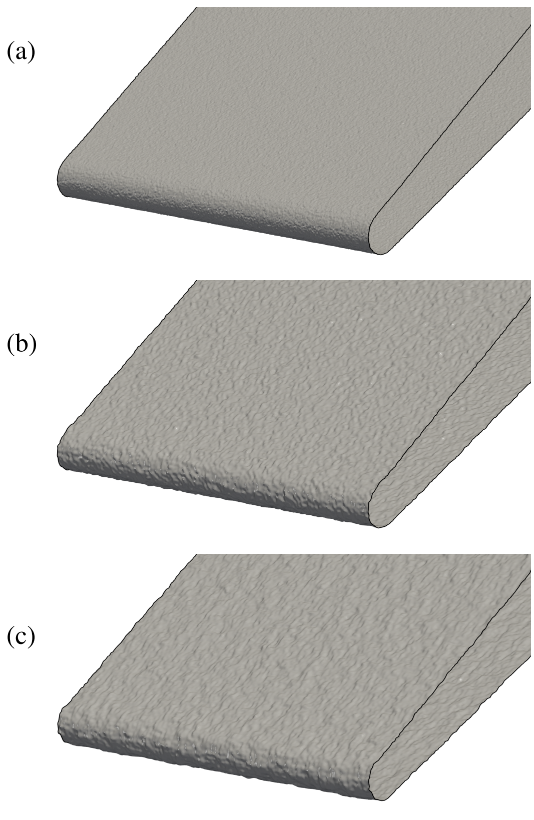

Figure 2. Close-up view of blade surface roughness on the HPT trailing edge (TE) for (a) small $(k_s/c = 1.0\times10^{-3})$; (b) intermediate $(k_s/c = 2.0\times10^{-3})$ and (c) large $(k_s/c = 3.0\times10^{-3})$ amplitude cases.

lence structures decorrelate to satisfactorily low levels. A compressible version of the Klein *et al.* (2003) digital filter method was used to synthesise isotropic inlet turbulence with an intensity of $T_u/U^i = 8\%$ and an integral length scale of $\mathscr{L}_x/c = 8\%$, where $T_u \equiv \sqrt{\frac{u'^2+v'^2+w'^2}{3}}$, and U^i is the axial velocity at the inlet. A non-reflective zonal characteristic boundary condition (Sandberg & Sandham, 2006) was enforced at the outlet, and Riemann invariant boundary conditions were used at the inlet. Periodic boundaries were imposed in the pitchwise (y) direction and the spanwise (z) directions.

In terms of the mesh dimensions, the background H-type grid for the smooth case was comprised of $(N_x\times N_y\times N_z) = 1470\times716\times384$ points, where N_x, N_y, N_z are the number of points in the axial, pitchwise and spanwise directions, respectively, whereas, for the rough cases, it had $(N_x\times N_y\times N_z) = 1470\times716\times576$ points. For the smooth case, the embedded O-type grid was comprised of $(N_1\times N_2\times N_3) = (6796\times254\times384)$ points, whilst for the $k_s/c = 0.001$ case it had $(N_1\times N_2\times N_3) = (6796\times254\times576)$ points, and, for the remaining $k_s/c = 0.002$ and $k_s/c = 0.003$ cases, it had $(N_1\times N_2\times N_3) = (6796\times358\times576)$ points. The grid spacings in the tangential, wall-normal, and spanwise directions normalised with the local viscous length scale $\delta_\nu = \nu/u_\tau$ are denoted as Δs^+, Δn^+, and Δz^+, respectively. Here $u_\tau = \sqrt{\tau_w/\rho}$ is the wall friction velocity with the wall shear stress τ_w and density ρ. The spanwise-then-time-averaged grid spacings on the surface of the smooth blade were found to be $\langle\Delta s^+\rangle \lesssim 7$, $\langle\Delta n^+\rangle \lesssim 0.5$ and $\langle\Delta z^+\rangle \lesssim 12$, which is slightly finer than the mesh resolution reported in past work by Zhao & Sandberg (2020). For the rough blades, the spanwise-then-time-averaged grid spacings were evaluated at the mean roughness height, which coincides with the coordinates of the smooth HPT blade, and were found to be $\langle\Delta s^+\rangle \lesssim 1.0$, $\langle\Delta n^+\rangle \lesssim 1.0$ and $\langle\Delta z^+\rangle \lesssim 10.0$ for all cases considered here.

To verify the accuracy of the BDIM algorithm in simulating flow past a smooth HPT vane, results from Pichler *et al.* (2017) and Zhao & Sandberg (2020) that used body-fitted computational grids and similar inlet turbulence intensities and integral length-scales were reproduced. The blade surface static pressure coefficient, C_p, and blade surface skin-friction coefficient, C_f, are compared in Figure 3 — good levels of agreement are observed between the body-fitted and BDIM data.

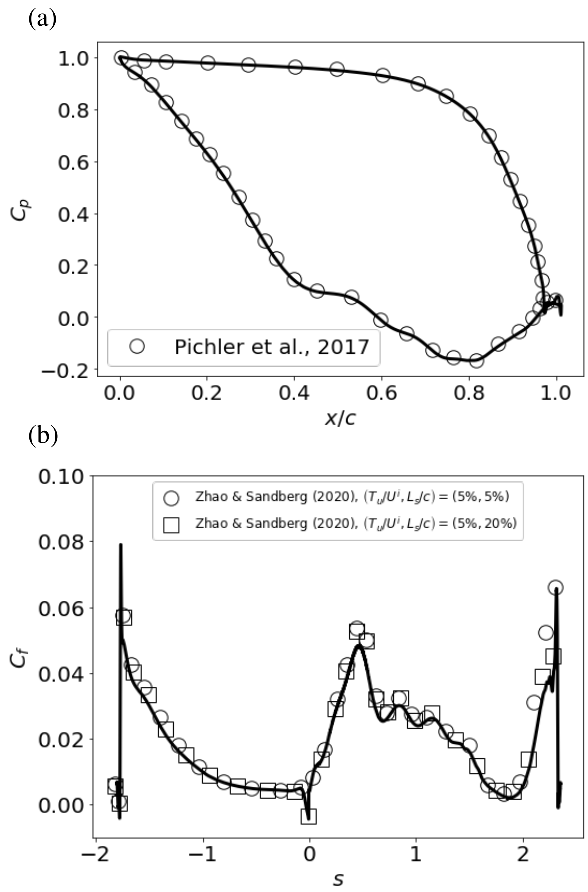

Figure 3. Validation against previous body-fitted HPT simulations performed by Pichler *et al.* (2017) and Zhao & Sandberg (2020) and current BDIM data (——). (a) Blade surface static pressure coefficient, C_p, plotted against axial position normalised by axial chord length, x/c. (b) Skin-friction coefficient, C_f, plotted against the the blade surface length, s, where $s > 0$ and $s < 0$ correspond to the SS and PS, respectively.

RESULTS

Two typical snapshots of the simulated flow-field are shown in Figure 4, which compares contours of instantaneous spanwise velocity (u_r) normalised by the axial time-averaged inlet velocity $(\overline{u}_x)$ on the axial-pitchwise $(x$-$y)$ plane for the smooth HPT blade (Figure 4a) and the intermediate roughness

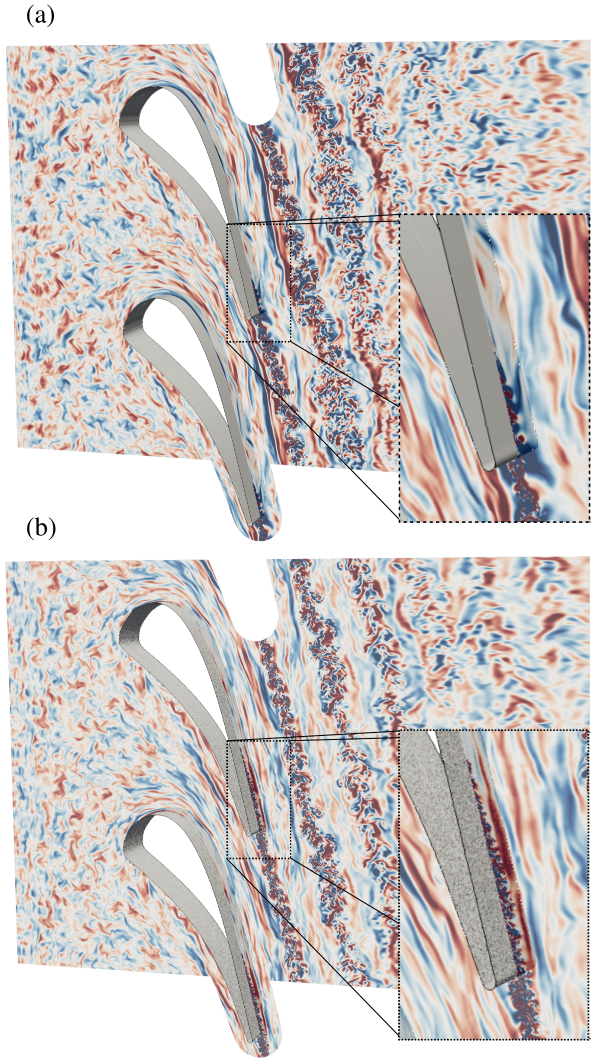

Figure 4. Contours of instantaneous spanwise velocity (u_z) normalised by the axial time-averaged inlet velocity ($\overline{u}_x$) at mid-span ($L_r/c = 0.2$) on the axial-pitchwise (x-y) plane (a) smooth HPT blade and (b) HPT blade with intermediate amplitude roughness ($k_s/c = 0.002$). Inset panel shows close-up view of boundary-layer transition of the blade suction side. Note that the computational domain has been copied twice in the pitchwise (y) direction.

case (Figure 4b) at mid-span ($z/c = 0.2$). Looking from left-to-right, a rich array of complex flow physics can be observed throughout the HPT cascade. These include: distortion and extension of freestream turbulence around the HPT leading-edge (LE) due to a curvature-driven favourable pressure gradient, pronounced vortex stretching in the HPT passage and boundary-layer transition on the blade suction-side (SS), as well as highly turbulent vortex shedding in the TE region that produces a wake with a broadband distribution of scales. The impact of blade surface roughness can be seen in the inset panels on Figure 4, which show close-up views of the SS blade boundary-layer in the TE region of the HPT blade. Comparing the boundary-layer development over the rough TE (Figure 4b) against that of the smooth (Figure 4a), it is clear that the flow over the rough surface not only undergoes an earlier transition to turbulence, but also contains finer-scale eddies whose size is commensurate with the topographical features of the underlying roughness distribution.

To further elucidate how the levels of surface roughness affects the blade boundary-layer development along the SS surface, the wall heat flux (WHF) and wall shear stress (WSS) were examined. The former quantity is defined here as

$$q = \frac{\mu}{Pr\,(\gamma-1)\,M^2}\frac{\partial T}{\partial n} \tag{1}$$

where Pr is the Prandtl number, γ is the heat capacity ratio, and M is the Mach number and $\partial T/\partial n$ is surface temperature gradient with respect to surface-normal direction. The WSS vector (in Cartesian coordinates) is defined here as

$$\vec{\tau}_w = \mu\left(\frac{\partial V_{t_1}}{\partial n}\vec{t}_1 + \frac{\partial V_{t_2}}{\partial n}\vec{t}_2\right) \tag{2}$$

where $\partial V_{t_1}/\partial n$ and $\partial V_{t_2}/\partial n$ are the wall-normal derivative of the tangential velocity with respect to $\vec{t}_1$ and $\vec{t}_2$, respectively. Here, attention is directed towards the wall-normal derivative of the tangential velocity with respect to $\vec{t}_1$, which can be written as $\partial V_{t_1}/\partial n = \left(\nabla\vec{V}^T\cdot\vec{t}_1\right)\cdot\vec{n}$, where $\vec{n}$ is the surface normal vector and where $\vec{t}_1$ is the tangential direction lying in the x-y plane with $\vec{t}_1\cdot\vec{i} \geq 0$, where $\vec{i}$ is the unit streamwise vector.

Contours of $\mu\partial V_{t_1}/\partial n$, and q on the SS surface of the smooth and roughened HPT blades are compared in Figure 5. The instantaneous data show that surface roughness introduces instabilities in the boundary layer along the whole span of the blade, which are not present on the smooth blade. These instabilities trigger an early transition to turbulence and the breakdown to turbulence occurs quicker, i.e., the transition point moves towards the LE, as the level of blade surface roughness increases. To be specific, whilst the transition onset appears to be confined to the final 15% of the SS surface for the smooth- and $k_s/c = 0.001$ cases, the boundary-layer is almost entirely turbulent along the entire length of the HPT vane for both the $k_s/c = 0.002$ and $k_s/c = 0.003$ cases. This observation is consistent with previous findings of Zhang & Ligrani (2006), who also noted a rapid breakdown to turbulence on the SS surface of roughened HPT blade with $k_s/c = 1.6\times10^{-3}$. Consequently, a markedly different transition mechanism occurs on the intermediate and large amplitude roughness blades considered here compared to the smooth-blade bypass transition discussed in past work by Zhao & Sandberg (2020). The fact that blade surface roughness can trigger such a rapid breakdown to turbulence implies that significant changes will also occur in the wake of HPT blade.

Figure 6a shows the effect of blade surface roughness on pitchwise profiles of turbulence kinetic energy (TKE) at 20% axial chord downstream of the TE. TKE is defined here as

$$k = \frac{1}{2}\overline{u_i'u_i'} \tag{3}$$

where u_i' is the turbulent velocity component. Whereas the TKE profiles of the smooth and small-amplitude roughness cases are practically indistinguishable from one another, the two remaining cases show some notable differences. For instance, relative to the smooth HPT blade, the peak TKE value increases by 8% and 32% for the intermediate- and large-amplitude roughness, respectively. The increase in the peak TKE value is accompanied by a widening of the profiles in the pitchwise direction as the blade surface roughness becomes

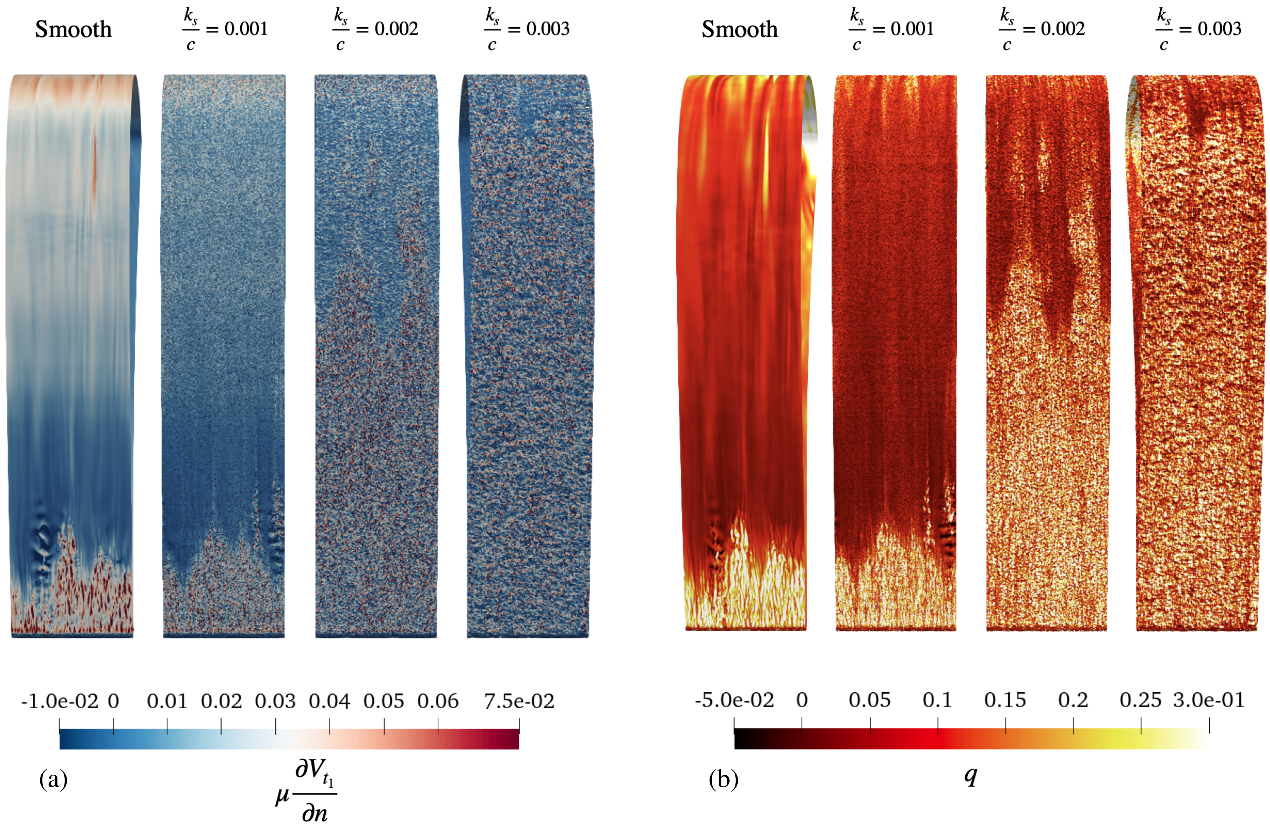

Figure 5. Spatial distribution of (a) instantaneous wall shear stress, $\mu \partial V_{t_1}/\partial n$, and (b) instantaneous wall heat flux, q, on the suction side of the smooth and roughened HPT blades.

larger. This increase in the fluctuations might be attributed to a higher turbulent kinetic energy production in the rough-wall boundary layer, which is advected downstream as the shear layer separated from the TE.

Pitchwise profiles of the kinematic wake loss, defined here as

$$\Omega(y) = \frac{p_{t1,mix} - p_{t2}(y)}{p_{t1,mix} - p_{2,mix}} \tag{4}$$

where $p_{t1,mix}$ and $p_{2,mix}$ are the mixed out stagnation pressure at the inlet and the mixed out static pressure at the outlet, respectively, and $p_{t2}(y)$ is the stagnation pressure, are plotted 20%C_{ax} downstream of the blade TE for each roughness amplitude are plotted in figure 6b. The kinematic wake loss increases as the non-dimensional roughness amplitude, k_s/c, increases. Relative to the smooth HPT vane, the peak value of the kinematic wake loss increases by almost 70% — underlying the significant impact that small-scale surface roughness have upon loss generation. Again, the increase in is apparent at peak value locations and is accompanied by increases in the width of the profiles as roughness size becomes larger. This is largely due to increased thickening of the boundary layers along the airfoil surfaces as increases. As noted by Ligrani (2012), possible explanations for the broader wakes with increased roughness size in Figure 6 could be (i) augmentations of mixing and turbulent transport in the boundary layers which develop along the roughened airfoils and / or (ii) increased turbulent diffusion in the transverse direction within the wake as it advects downstream. A detailed interrogation of (i) and (ii) is in progress.

CONCLUSIONS

The effects of blade surface roughness upon HPT performance and heat transfer has been studied using highly-resolved LES at an exit Reynolds and Mach number of 590,000 and 0.9, respectively. Three roughness amplitudes have been investigated, namely, $k_s/c = \{1.0, 2.0, 3.0\} \times 10^{-3}$ (figure 2), where k_s is an equivalent value of Nikuradse's sand-grain roughness for an irregular near-Gaussian roughness topography. The rough HPT geometries were represented using a boundary-data immersion method (BDIM) in conjunction with a two-block overset mesh configuration (figure 1), which was validated against existing simulation data that used body-fitted smooth HPT geometries (figure 3).

Whilst it is well-known that blade surface roughness can significantly affect aero-thermal performance, relatively to aerodynamically smooth blades, several questions regarding the fundamental mechanisms that govern pressure losses and heat transfer remain open. The results presented here highlight the strong impact that blade surface roughness has upon laminar-turbulence transition on the suction surface (figure 4), which, in turn, affects the wall shear stress and wall heat flux (figure 5), as well as the levels turbulence kinetic energy and total pressure losses in the wake (figure 6). Ongoing work is focussing on associating particular physical mechanisms to changes in aero-thermal performance, such as mean viscous dissipation and turbulent wall heat flux.

ACKNOWLEDGMENTS

The presented data were obtained using resources of the Oak Ridge Leadership Computing Facility at the Oak Ridge

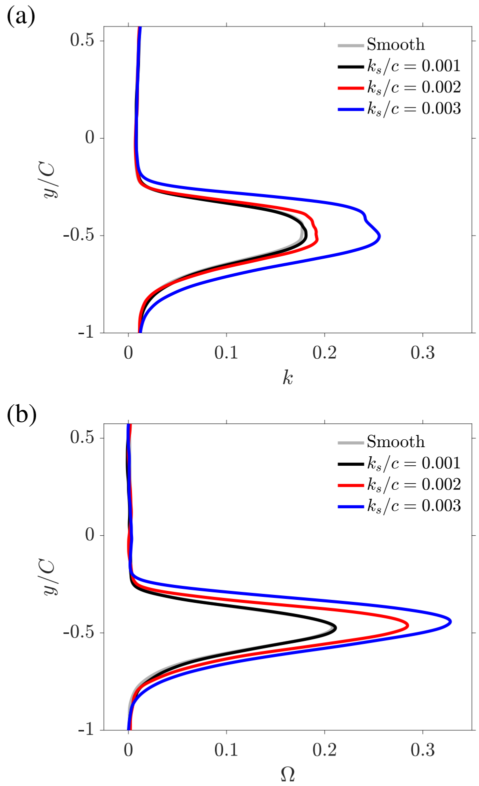

Figure 6. Pitchwise profiles of (a) turbulence kinetic energy (k) and (b) kinematic wake loss (Ω). Both profiles are shown 20% axial chord downstream of the blade TE.

National Laboratory, which is supported by the Office of Science of the U.S. Department of Energy under Contract No. DE-AC05-00OR22725.

REFERENCES

Bhaskaran, R. & Lele, S. K. 2010 Large eddy simulation of free-stream turbulence effects on heat transfer to a high-pressure turbine cascade. *J. Turbul.* **11**, N6.

Bons, J. P. 2002 St and Cf augmentation for real turbine roughness with elevated freestream turbulence. In *Turbo Expo: Power for Land, Sea, and Air*, , vol. 36088, pp. 349–363.

Bons, J. P. 2010 A Review of Surface Roughness Effects in Gas Turbines. *J. Turbomach.* **132** (2), 021004.

Hammer, F., Sandham, N. D. & Sandberg, R. D. 2018 Large Eddy Simulations of a Low-Pressure Turbine: Roughness Modeling and the Effects on Boundary Layer Transition and Losses. In *Turbo Expo: Power for Land, Sea, and Air*, , vol. 51005, p. V02BT41A014.

Han, Je-Chin, Dutta, Sandip & Ekkad, Srinath 2012 *Gas turbine heat transfer and cooling technology*. CRC press.

Jee, S., Joo, J. & Medic, G. 2016 Large-eddy simulation of a high-pressure turbine vane with inlet turbulence. In *Turbo Expo: Power for Land, Sea, and Air*, , vol. 49729, p. V02DT44A019.

Jelly, T. O. & Busse, A. 2018 Reynolds and dispersive shear stress contributions above highly skewed roughness. *J. Fluid Mech.* **852**, 710–724.

Jelly, T. O. & Busse, A. 2019 Multi-scale anisotropic rough surface algorithm: Technical documentation and user guide. *Tech. Rep.*. University of Glasgow.

Joo, J., Medic, G. & Sharma, O. 2016 Large-eddy simulation investigation of impact of roughness on flow in a low-pressure turbine. In *Turbo Expo: Power for Land, Sea, and Air*, , vol. 49712, p. V02CT39A053.

Klein, M., Sadiki, A. & Janicka, J. 2003 A digital filter based generation of inflow data for spatially developing direct numerical or large eddy simulations. *J. Comp. Phys.* **186** (2), 652–665.

Ligrani, P. 2012 Aerodynamic losses in turbines with and without film cooling, as influenced by mainstream turbulence, surface roughness, airfoil shape, and Mach number. *Int. J. of Rotating Mach.* **2012**.

McClain, S. T., Hanson, D. R., Cinnamon, E., Snyder, J. C., Kunz, R. F. & Thole, K. A. 2021 Flow in a Simulated Turbine Blade Cooling Channel With Spatially Varying Roughness Caused by Additive Manufacturing Orientation. *J. Turbomach.* **143** (7), 071013.

Michelassi, V., Martelli, F, Dénos, R., Arts, T. & Sieverding, C. H. 1998 Unsteady heat transfer in stator-rotor interaction by two equation turbulence model. In *Turbo Expo: Power for Land, Sea, and Air*, , vol. 78620, p. V001T01A058.

Nicoud, F. & Ducros, F. 1999 Subgrid-scale stress modelling based on the square of the velocity gradient tensor. *Flow Turbul. Combust.* **62** (3), 183–200.

Pichler, R., Sandberg, R. D., Laskowski, G. & Michelassi, V. 2017 High-fidelity simulations of a linear HPT vane cascade subject to varying inlet turbulence. In *Turbo Expo: Power for Land, Sea, and Air*, , vol. 50787, p. V02AT40A001.

Pichler, R., Sandberg, R. D., Michelassi, V. & Bhaskaran, R. 2016 Investigation of the accuracy of RANS models to predict the flow through a low-pressure turbine. *J. Turbomach.* **138** (12), 121009.

Sandberg, R. D. & Michelassi, V. 2022 Fluid Dynamics of Axial Turbomachinery: Blade-and Stage-Level Simulations and Models. *Annu. Rev. Fluid Mech.* **54**, 255–285.

Sandberg, R. D., Michelassi, V., Pichler, R., Chen, L. & Johnstone, R. 2015 Compressible direct numerical simulation of low-pressure turbines, Part I: Methodology. *J. Turbomach.* **137** (5), 051011.

Sandberg, R. D. & Sandham, N. D. 2006 Nonreflecting zonal characteristic boundary condition for direct numerical simulation of aerodynamic sound. *AIAA Journal* **44** (2), 402–405.

Schlanderer, S. C., Weymouth, G. D. & Sandberg, R. D. 2017 The boundary data immersion method for compressible flows with application to aeroacoustics. *J. Comp. Phys.* **333**, 440–461.

Stripf, M., Schulz, A. & Bauer, H.-J. 2008 Modeling of Rough-Wall Boundary Layer Transition and Heat Transfer on Turbine Airfoils. *J. Turbomach.* **130** (2), 021003.

Vadlamani, N. R., Tucker, P. G. & Durbin, P. 2018 Distributed roughness effects on transitional and turbulent boundary layers. *Flow Turbul. Combust.* **100** (3), 627–649.

Zhang, Q. & Ligrani, P. M. 2006 Numerical predictions of Stanton numbers, skin friction coefficients, aerodynamic losses, and Reynolds analogy behavior for a transsonic turbine vane. *Numer. Heat Transf.; A: Appl.* **49** (3), 237–256.

Zhao, Y. & Sandberg, R. D. 2020 Bypass transition in boundary layers subject to strong pressure gradient and curvature effects. *J. Fluid Mech.* **888**, A4.

Zhao, Y. & Sandberg, R. D. 2021 High-Fidelity Simulations of a High-Pressure Turbine Vane Subject to Large Disturbances: Effect of Exit Mach Number on Losses. *J. Turbomach.* **143** (9), 091002.